Nanoscale

Accepted Manuscript

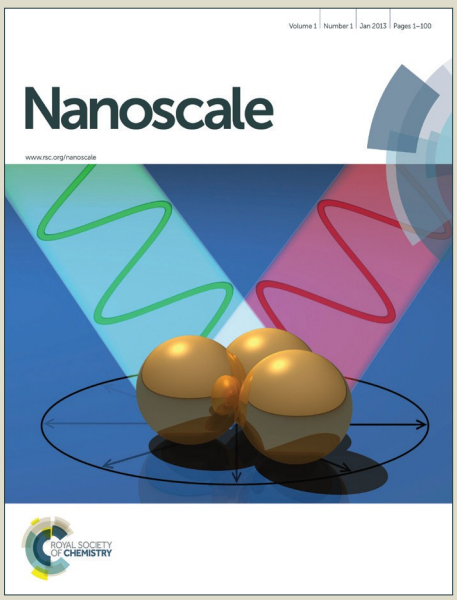

ROYAL SOCIETY OF CHEMISTRY

www.rsc.org/nanoscale

Nanoscale

ARTICLE

Detection of quantum well induced single degenerate-transition-dipoles in ZnO nanorods

Received 00th January 20xx,
Accepted 00th January 20xx

DOI: 10.1039/x0xx00000x

www.rsc.org/

Siddharth Ghosh[a, †], Moumita Ghosh[b, c, d, †], Michael Seibt[d], G Mohan Rao[c]

Quantifying and characterising atomic defects in nanocrystal is difficult and low-throughput using the existing methods such as high resolution transmission electron microscopy (HRTEM). In this article, using defocused wide-field optical imaging technique, we demonstrate that single ultrahigh-piezoelectric ZnO nanorod contains a single defect site. We model the observed dipole-emission patterns from optical imaging with a multi-dimensional dipole and find that the experimentally observed dipole pattern and model-calculated patterns are in excellent agreement. This agreement suggests presence of vertically oriented degenerate-transition-dipoles in vertically aligned ZnO nanorods. HRTEM of this ZnO nanorod shows presence of a stacking fault, which generates a localised quantum well induced degenerate transition dipole. Finally, we elucidate that defocused wide-field imaging can be widely used to characterise defects in nanomaterials to answer many difficult questions towards the performance of low-dimensional devices such as energy harvesting, advanced metal-oxide-semiconductor storage, nanoelectromechanical and nanophotonic devices.

1 Introduction

Localising and studying physical properties of single defect sites in high-aspect-ratio nanostructures such as nanorods or nanowires at atomic resolutions are cumbersome tasks using available technologies. We confront the same problem while studying defect induced enhanced-piezoelectricity of ZnO nanorods. To overcome this problem, we used a simple however an efficient approach of optical microscopy. The fundamental motivation of this work was to understand the structural and electronic properties of crystal defect in ZnO nanorods while recognising the reason behind its ultra-high piezoelectricity. From the material science perspective, zinc oxide is one of the extensively researched lead free piezoelectric materials. At nanoscale dimension, it has low piezoelectric response than compare to the other piezoelectric nanomaterials.[1,2] Recently, that was overcome and the highest reported d_{33} value for undoped ZnO nanorod was found to be 44.33 pm/V.[3] It was also found that these wurtzite ZnO nanorods are ferroelectric in undoped condition whereas, it is well known that wurtzite ZnO is intrinsically non-ferroelectric.[4,5] Here, the reason behind the ferroelectricity was due to a stacking fault induced electronic charge imbalance in the *c*-plane. This stacking fault was studied with high resolution transmission electron microscopy (HRTEM). The HRTEM has atomic resolution however, the problem lies while searching and quantifying defects in long nanostructures. It is rather low-throughput and area of field of view dependent (at certain magnification). In addition, distinguishing structural defect under HRTEM is dependent on the angle of electron beam interaction. To circumvent these typical problems, we demonstrate a powerful approach of quantifying stacking faults with electronic property information using defocused optical imaging for ZnO nanorods. The study reveals that stacking fault generated quantum well (QW) exhibits single transition dipole in these single ZnO nanorods with degenerate energy level.

The defect generated electron-hole pair that oscillates at THz frequencies and emits a distinct wavelength of photon is widely known as transition emission dipole. Due to the intrinsic relation between defect and transition dipole, one can study the

[a] *III. Institute of Physics, Georg-August-Universität-Göttingen, Friedrich-Hund-Platz 1, 37075 Göttingen, Germany.*
[b] *Centre for Nano Science and Engineering, Indian Institute of Science, Bangalore 560012, India*
[c] *Instrumentation and Applied Physics, Indian Institute of Science, Bangalore 560012, India.*
[d] *IV. Institute of Physics, Georg-August-Universität-Göttingen, Freidrich-Hund-Platz 1, 37075 Göttingen, Germany.*
† Corresponding authors: ghoshiisc@gmail.com, sghosh@physik3.gwdg.de

Electronic Supplementary Information (ESI) available: [Details of hydrothermal growth of ZnO nanorods, ferroelectric characterisation, defocused imaging setup and parameters, sample preparation for defocused imaging, fundamental of dipole modelling, photoluminescence images with issues of spatial distribution and XRD confirmation of zinc-blend stacking fault are described in the supporting information.]. See DOI: 10.1039/x0xx00000x

number of transition dipoles[6,7] to determine the concentration of defects per nanostructure. Here, such photoluminescence (PL) is observed in the green wavelength besides ZnO's identifying characteristic near-band-emission (NBE) peak in the UV range. The green emission or the deep-level-emission (DLE) in ZnO generally corresponds to excitons generated from oxygen vacancy or zinc vacancy or zinc interstitial defects.[8,9,10] However, PL spectrum cannot quantify the concentration of defect centres. Typically, one way of determining number of single emitters is photon antibunching.[11,12] However, in antibunching technique photon counts per time should be very high and if there is agglomeration of more than one single emitter, which is unlikely to avoid, then it gives rise to unreliable results. In the end, many trials are needed to get the best antibunching dip at zero delay time. Antibunching of II-VI semiconductor nanostructure (specifically ZnO nanorods) was demonstrated earlier proving the presence of single photon source[13] from single defect.[14,15] To evade the aforementioned problems and quantify the number of dipole-emitters in a simple but in an exemplarily high-throughput way, we have carried out defocused imaging of ZnO nanorod using a wide-field optical microscope to obtain the defocused pattern of emitting dipole. The distinct and unique defocused patterns of dipole emitters not only determine the number of dipoles but also resolve the angular orientation of them. Defocused imaging of single non-degenerate-transition-dipole and degenerate-transition-dipole emitters were earlier reported using position dependent energy flux method with multidimensional dipole modelling for single molecules and other nanomaterials.[16-21] It is an efficient method to determine the quantity and orientation of dipole emitters. However, it has never been applied as an essential tool to characterise defects in material science and to extract significant potential answers for physical questions, such as in our case — why this particular ZnO is ultra-high-piezoelectric?

Here, using defocused optical imaging we demonstrate the presence of quantum well induced degenerate-transition-dipole in these ZnO nanorods. By defocusing the optics, we captured the defocused dipole patterns, which are the space distribution of emission field of dipoles on the detection plane of electron multiplying charged coupled device (EMCCD). The defocused patterns are compared with multi-dimensional dipole modelling simulation. This comparison determines the number of single transition dipoles and their orientations. Here, the ZnO nanorods have *c*-axis directed vertical growth on substrate.[3] During the defocused imaging *c*-axes of the nanorods were parallel to the optical axis. Therefore, the defocused pattern found on the EMCCD plane should be the angular distribution relative to the vertical orientation of the nanorods. From the quantification and orientation of dipoles, we infer that single defect site with vertically oriented degenerate-transition-dipole is present in every single ZnO nanorod.

2 Methods

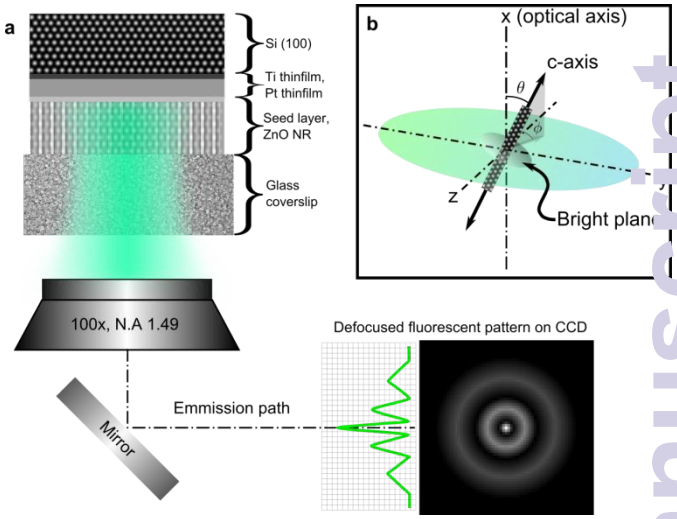

Figure 1. Defocused optical wide-field imaging of ZnO nanorod. **a.** The ZnO nanorods were grown on a seed layer thin-film of ZnO, platinum and titanium coated on (100) silicon wafer. The ZnO nanorods in the aforementioned configuration were vacuum bonded with clean gl coverslip. So, the nanorods were vertically oriented with the glass coverslip. Here, the excitation wavelength was 488 nm. An oil immersion high numerical aperture (1.49) was used to collect th complete piezo-stage manipulated defocused pattern onto 1024x1024 EMCCD chip. **b.** Euler angle distributions of nanorod. In the spheric coordinate systems, *z* is considered as optical axis. Any angula deviation of *c*-axis of the nanorod from optical axis is denoted as When, θ is zero, all the points on the *c*-axis will converge to the optic axis and finally, φ is the azimuthal angle from *y*-axis.

2.1 Defocused optical wide-field imaging – Experimenta modelling

The ZnO nanorods were grown on a stack of thin-film nanomaterials according to the earlier reported hydrotherma growth by Ghosh et al.[3] The schematics shown in Fig. 1a and 1b demonstrate the configuration of such nanorods within e spherical coordinates. These nanorods are vertically aligned with respect to the optical axis. So, for perfectly vertical nanorods, the *c*-axis of the nanorod should have angula deviation of $\theta = 0°$ with respect to the optical axis (*z*). To obtain the defocus pattern of emission dipole at room temperature (23 °C) and atmospheric pressure, an Olympu 100× objective lens with high numerical aperture (NA) of 1.49 was used. In order to defocus the emitter from the focal plan the objective lens was displaced with a piezo-stage-manipulator (PIFOC, Physik Instrumente, Germany) along the *z* ax towards the detector plane (see supporting information – Fig. S1). We calculate the position dependent energy flux densit through the EMCCD plane. At this plane, the flux is proportional to the perpendicular component of the Poyntin vector[16]. Here, the dipole does not have typical electrodynami interaction with the glass-air interface. It is inside the 550 nm long ZnO nanoro

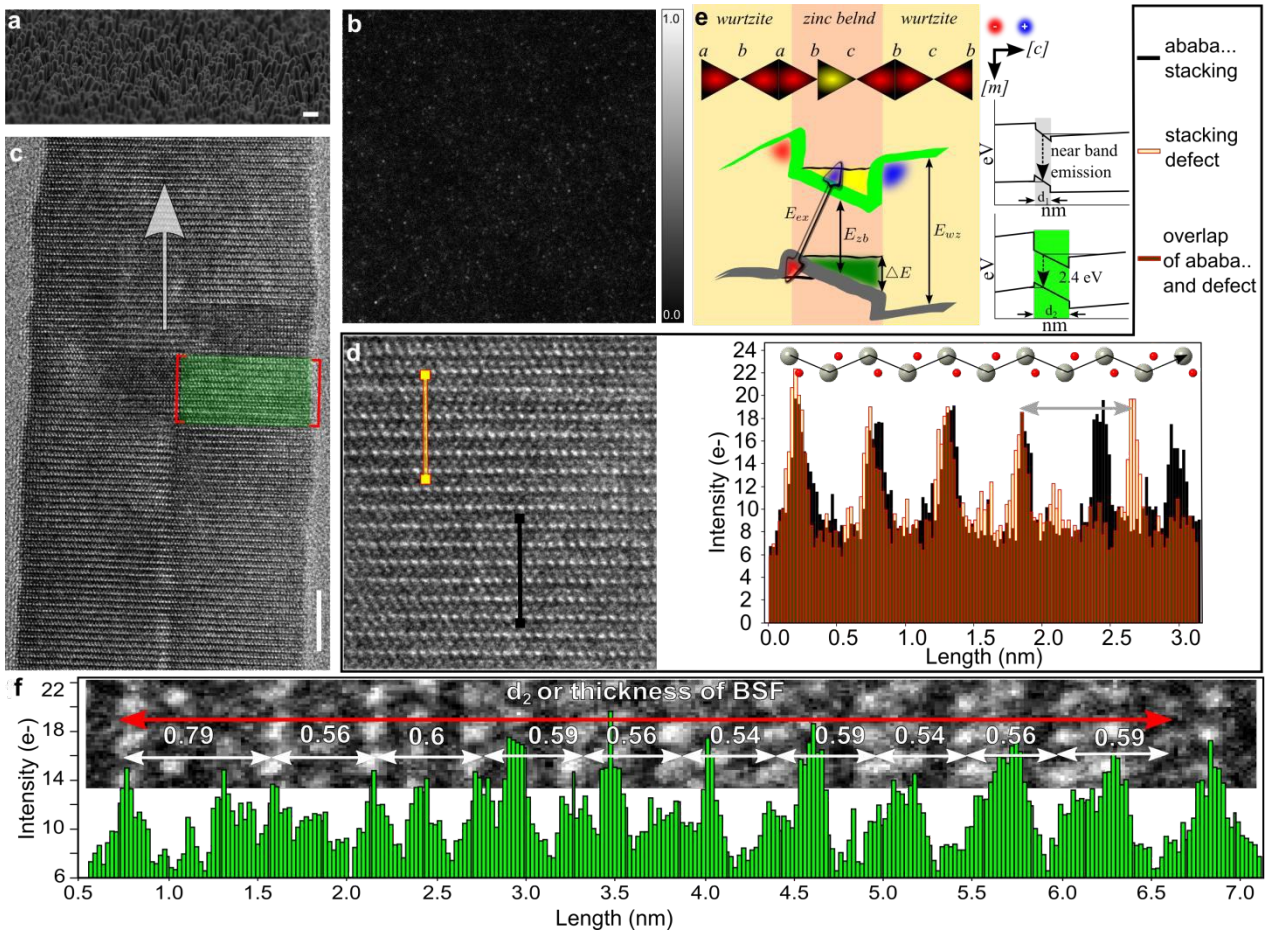

Figure 2. Vertically aligned ZnO nanorod with stacking defect. **a.** Tilted scanning electron microscopic image of vertical aligned ZnO nanorod with 200 nm scale bar. **b.** Focused wide-field photoluminescence intensity image. **c.** High Resolution Transmission Microscopic (HRTEM) image of nanorod shows high crystallinity and growth direction along *c*-axis. The stacking fault region is highlighted with green rectangle. This region is magnified in *d* (along with defect free region) and *f* for defect analysis. The scale bar represents 5 nm. **d.** The electron intensity plot comparing wurtzite region and stacking fault initiating region. The magnified HRTEM is angle-corrected (ϕ) for +1.4° . The black line profiles *ababa* ··· stacking of ZnO. The intensity peaks of atomic positions of *ababa* ··· stacking corresponds to the simulated atomic arrangements. The light-yellow red bordered line profiles the initiation of stacking fault. The plot shows distinct disordered periodicity from 1.86 to 2.65 nm (δ = 0.79 nm). The grey arrow indicates this region in the intensity plot. At this region, perfect overlapping of two plots is missing. The black plot maintains the periodicity of ababa... crystallinity. **e.** Presence of the stacking fault has created a localised quantum well at wurtzite/zinc-blend/wurtzite interface with an energy difference of ΔE from energy of wurtzite (E_{wz}) to energy of zinc blend (E_{zb}) and resulted in excitation energy of E_{ex} [24]. Transition energy of this kind of QW is dependent on the thickness of the stacking fault region, explained using d_i as the effective electronic thickness or the thickness of the BSF. Here $d_2 > d_1$, which shifts transition energy from NBE to DLE . **f.** Line profile of the BSF region with corresponding HRTEM in background. Here, the stacking fault continued for 5.5 nm (with more than 5.22 Å lattice parameter as shown with white arrows), which is considered as effective electronic thickness d_2.

Table 1. Parameters for multi-dimensional dipole model (supporting information). Figure 4d and 4e are calculated based on the polar angular deviation of θ from the optical axis, azimuthal angle φ, the ratio of bright plane dipoles' intensity $I_x:I_y = I_{xy}$, the ratio of bright plane dipole intensity to intensity of vertical dipole $I_{xy}:I_z$ and the defocusing height from the focal plane δz.

Calculated Figure	θ (°)	φ (°)	$I_x:I_y = I_{xy}$	$I_{xy}:I_z$	δz (nm)
4d	0	0	1	0.8	839
4e	11	126	1	0.8	845

On top of the nanorod there is a stack of thin-films as illustrated in Fig. 1a. The particulars of the thicknesses and considered refractive indices used in further calculations are mentioned in the supporting information. Later, we show that the observed dipole pattern refers to certain degeneracy in the energy levels. To calculate the degenerate-transition-dipole, we considered three perpendicular linear emission dipoles (*dx*, *dy*, *dz*) in three spatial directions at a single point; in short, it is their superposition (see supporting information – Fig. S1). The variable intensities of three dipoles *dx*, *dy* and *dz* are assumed to be I_x, I_y, and I_z, respectively. All the experimental parameters as mentioned in table 1 were known, except

intensity ratios of the three considered dipoles. The ratios of the intensities were determined from the calculation by maintaining the other experimental parameters constant. To calculate the image on the detector plane, the intensity ratio of *dx* and *dy* dipoles (I_x:I_y = I_{xy}), intensity ratio of I_{xy} to d_z dipole (I_{xy}:I_z), defocusing height (δz), angle of deviation from the optical axis (θ) and azimuthal angle (φ) are considered according to the measurement conditions and are mentioned in table 1.

3 Results and discussion

3.1 SEM and PL imaging of vertically aligned ZnO nanorods

The morphology of vertically aligned ultra-high-piezoelectric ZnO nanorods is showed in Fig. 2a. These nanorods were optically excited with 488 nm wavelength and their emission wavelength was 525 nm (supporting information - Fig. S2). This green emission is due to the trapped excitons in the stacking fault of ZnO nanorods.[22,23] We observe in-plane spatial density of these emitters in the photoluminescent wide-field image as shown in Fig. 2b. Blinking behaviour of the nanorod enables capturing sparse single transition dipole at fast exposure duration. The slow imaging or long exposure images agree well with the SEM like density of ZnO nanorods as shown in supporting information (Fig. S3) where discrete and individual single-emitters can hardly be observed.

3.2 Effect of basal stacking fault on band-gap

We observe crystalline atomic arrangements of ZnO from the HRTEM. The *ababa…* stacking of zinc and oxygen are observed in Fig. 2c. The HRTEM analysis in Fig. 2d shows a basal plane stacking fault where, a stack of atoms is distinctly missing or shifted, which leads to an atomic lattice misalignment. This defect discontinues the *ababa…* stacking symmetry of ZnO. The typical lattice constant of ZnO observed from the HRTEM along the *c*-axis is 5.22 Å. However, the distance between two consecutive atomic intensity peaks is separated by 7.94 Å (Fig. 2d) at the missing atomic layer site, where zinc blend crystallinity is initiated. In Fig. 2e, we show the band-gap energy difference ΔE is due to the two interfacial crystalline structures ─ wurtzite (E_{wz}) and zinc-blend (E_{zb}) (supporting information ─ Fig. S4); and the stacking fault considered here is *I1* type for II-VI wurtzite semiconductor.[24] This *I1* type basal stacking fault (BSF) continued for 5.5 nm with lattice parameter more than 5.22 Å as shown in Fig. 2c and 2f. In Fig. 2c the total BSF region is highlighted with green and in Fig. 2f a line profile of this region is plotted to quantitatively analyse the continued lattice mismatch resulting to a localised hetero-structure. The effective electronic thickness (d_i – Fig. 2e) of the total BSF distance (5.5 nm) influences the band alignment as shown in Fig. 2e. It is inevitable when d_i increases (d_2>d_1) a red shift of transition energy from NBE to DLE should be observed.[24] Due to such localised lattice mismatch, a quantum confinement of exciton is observed with a band alignment of 2.36 eV when the distance of the quantum well is 5.5 nm. The localised quantum well generates a vertical degener transition dipole at the stacking fault, which is situated in th *c*-plane (Fig. 3).

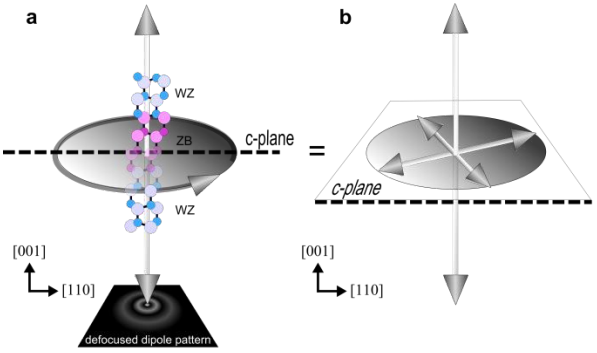

Figure 3. a. Single degenerate transition dipole inside the basal stac ng fault region where zinc blend crystallinity is observed. The stacking fault is situated in the c-plane, which provides the distinct vertical orientatio the circular degenerate dipole. **b.** The circular degenerate dipole can be considered as superposition of three vertical dipoles to calculate the dipole pattern.

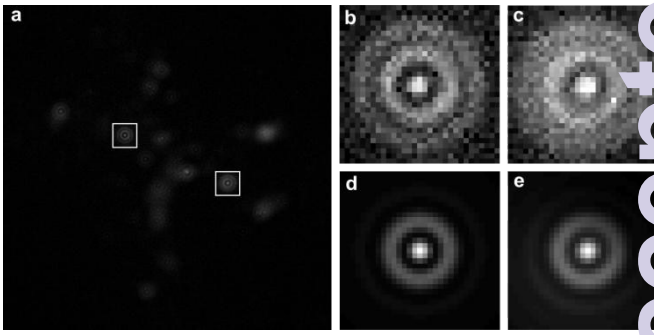

Figure 4. Defocused emission pattern of ZnO nanorods. **a.** Collectiv defocused patterns of ZnO nanorods at total 160× magnification, 512x cropped region from the EMCCD. A less dense region was found to capture quality defocused imaging. The white marked patterned are digitally zoomed in **b**, **c**. and compared with the calculated defocused image in **d**, **b** and **d** are in good agreement. The calculation has considered the measurement conditions. **d.** uses intensity ratio of *x* and *y* dipole (I_x:I_y = I_{xy}) as 1, intensity ratio of I_{xy} to z dipole (I_{xy}:I_z) = 0.8, defocusing height (δz) f 839 nm, θ=0° and φ =0°. e. uses I_{xy} as 1, I_{xy}:I_z = 0.8, δz of 839 nm, θ=11° and φ =126°.

3.3 Orientation and number of dipoles

The wide-field defocused pattern of emission dipoles shown in Fig. 4a was recorded using 30 s exposure time of an EMCC camera (see supporting information), which was synchronised with a pulsed laser excitation . The measured defocuse images correspond to multiple degenerate energy levels o perfect degenerate-transition-dipole. Here, the ratio of I_{xy} to is found to be 0.8 ─ 0.85. The calculated images show excellent agreement with the measured defocused images. two specific defocused patterns in Fig. 4b and Fig. 4c a

compared with the calculated defocused images in Fig. 4d and Fig. 4e, respectively for the particular given measurement conditions. The modelled dipole pattern of Fig. 4b i.e. Fig. 4d shows that the θ and φ both were at 0° for the dipole. So, the degenerate dipole was vertical ─ facing the optical axis and situated in the c-plane basal stacking fault. In Fig. 3a, we schematically explain the behaviour of the vertical degenerate dipole that is situated inside the basal stacking fault. The degeneracy generated plane-emission of the dipole, which is widely considered as a circular dipole can be approximated as with planar dipoles as shown in Fig. 3b. The vertically oriented degenerate dipole (Fig. 3a) is equivalent to superposition of three dipoles, which are perpendicular to each other as shown in Fig. 3b (more details in supporting information). The schematic in Fig. 3 explains the reason behind the dipole's vertical orientation, which is observed in all defocused pattern. Furthermore, in isolated nanorods we do not observe any overlapped pattern of other dipoles. This confirms presence of single degenerate dipole emitter in each single nanorod. It is observed in the SEM and wide-field focused images (Fig. 2a and 2b) that growth of the nanorods is very dense. Therefore, to avoid overlapping of defocused patterns (see supporting information) of different nanorods, we selected a least densely populated area of nanorods. Also in Fig. 4c and Fig. 4e, we do not observe presence of multiple emitters. Here, θ and φ were at 11° and 126°, respectively. From the SEM (Fig. 2a), we notice that some nanorods have slight polar-angular deviation. The small deviation of θ from the optical axis of the dipole is because of the angular orientation of the nanorods that is purely structural. In total, 37 defocused images were analysed to determine the distributions of polar and azimuthal angles. At θ = 0, the *c*-axis of the nanorods are perpendicular to the coverslip ─ vertically oriented nanorods.

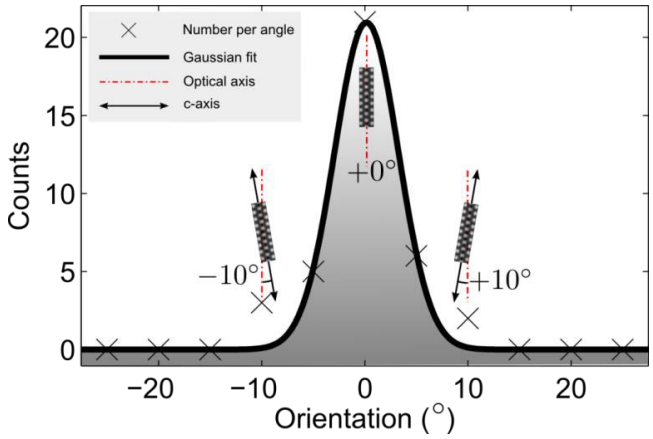

Figure 5. Angular distribution of nanorods. Here, *y*-axis denotes number of nanorods in terms of counts and *x*-axis for the angular orientation of the dipole (θ). 21 vertical defocused patterns were found in 50x50 μm^2 area. The maximum angular deviation was found to be ±10°.

We observe polar-angle (θ) variation of the nanorods for a 50×50 μm^2 area in Fig. 5. On average, 21 (±2.1) nanorods had perfect single vertically oriented degenerate-transition-dipole and maximum angular deviation of ±10° was observed for the remaining 16 patterns. Such angular distributions of the dipoles are due to structural geometry of the nanorods. This infers that the dipole is situated in the stacking fault that perpendicular to the *c*-axis as well as to the optical axis.

The degeneracy found in the patterns is because of the intrinsically degenerate and anisotropic valence band of ZnO.[25] Therefore, the degeneracy is also observed in the excited state of the trapped exciton in basal stacking fault of ZnO nanorods, which is similar to CdSe.[26] These confined excitons in the stacking fault of II-VI wurtzite semiconductor nanostucture result into a localised quantum well.[24,27,28,29] It is true that degeneracy generated plane-polarised emission (or circular dipole) vanishes while the structural aspect-ratio of nanocrystals increases along the *c*-axis.[30] This is only effective when the quantum confinement is strongly dependent on the global length-scale of the nanocrystal. On the contrary, in our case the confinement is localised at the BSF generated lattice mismatch, so the robust degeneracy[25,31] is not broken. Stacking fault in wurtzite semiconductor occurs due to several reasons[32]. One of them is vacancies of both zinc and oxygen[32], which discontinue the innate crystallinity to establish a local heterogeneity of different crystallinity. PL and X-ray diffraction (XRD) characteristics also confirm that no element other than the zinc and oxygen are present in ZnO nanorods (supporting information – Fig. S2 and S4). Another investigation of energy dispersive spectroscopy (supporting information – Fig. S5) under HRTEM also agrees well with the presence of zinc blend stacking fault. So, here the vacancies of these two atoms are the reason behind the generation of stacking fault.

The defocused pattern defines the geometry and the angle of orientation of the dipole. By analysing the defocused pattern of the dipole, we confirm that the dipole is situated in the *c*-plane and oscillating along the *c*-axis as indicated by the presence of in-plane electric field vector components (Fig. 3 and 4). This substantiate that the origin of the green emission is from the stacking fault situated at the *c*-plane. The orientation and *z*-axis position of the dipole matches well with the HRTEM observation. One may argue that the dipole is from random oxygen point defects. In that case, we should not have observed reproducible vertically oriented dipole in all the nanorods, instead we should have observed random angular distributions, which is not the case here. Besides, the calculated defocused patterns use defocusing heights (δz), which agrees well with the *z*-axis position of the stacking fault (supporting information). The laser used here has a Gaussian intensity profile, so the maximum intensity of dipole can be found at the centre of the image frame. Also the variation in intensities of the dipoles at certain captured duration of frame is because of their independent and incoherent blinking behaviour, which limits the uniform number of photon acquisition per dipole. The similar defocused pattern of the dipole and its emission wavelength confirm that each of the ZnO nanorods contain similar kind of defect.

4 Conclusions

In summary, we have shown that the undoped, highly crystalline and ultrahigh piezoelectric ZnO nanorod has a single degenerate-transition-dipole site. We used a simple but efficient technique to detect the number of degenerate-transition-dipoles. The ZnO nanorods presented here are luminescent at 525 nm. A thorough HRTEM analysis confirms presence of BSF region in ZnO nanorod with total effective electronic thickness of 5.5 nm resulting in DLE. In the HRTEM study, this defect is prominently visible at the *c*-plane or at the 'bright plane' that is perpendicular to the *c*-axis of the ZnO nanorod. However, exploring single defect under HRTEM is tedious when the nanostructure is 500-550 nm long. So, we decided to study the number of defect induced transition-dipoles per nanorods. Using defocused imaging approach one can simultaneously observe individual behaviour of many single low-dimensional materials distributed on a large area. The Defocused wide-field images collected with high numerical aperture on EMCCD plane for longer exposure allowed us to capture the out-of-focal-plane spatial distribution of electromagnetic wave-fronts. This generates certain pattern of dipoles containing information such as number of dipoles and their orientations. The measured defocused patterns were correlated with numerically simulated images. In the calculation, we considered all the experimental conditions and took care of the multi-stacked material properties above the nanorods ─ the refractive indices and their thicknesses. The uniform distribution of the defocused patterns in *x*-*y* plane or at *c*-plane confirms presence of a vertical dipole per single nanorod. However, a single oscillating non-degenerate vertical transition dipole should never produce high intensity photonic peak at the centre of the pattern. The opposite is observed in all the dipole patterns, which confirm that the defocused pattern is not from a purely single non-degenerate dipole emitter. We found a high intensity peak in the centre of the defocused pattern along with the in-plane vector components confirming that it is a superposition of three perpendicular dipoles, which can be possible due to the degeneracy of a transition dipole with vertical orientation. The primary aim of the study was to determine, how many emission dipoles are present in the nanorods to quantify the defect centres.

Finally, this efficient characterisation to determine the number, orientation and electronic properties of transition dipoles classifies this particular ZnO nanorod as a single BSF induced piezoelectric energy harvesting nanomaterial. When a wide range of material scientists are struggling with tedious experimental and quantum mechanical calculations to understand the electronic properties of crystal defects, we present a simple experimental technique accompanying with a semi-classical numerical calculation. We envision that defocused optical wide field imaging method would be a powerful way of characterising defects in nanocrystals or crystalline thin-films to quantitatively analyse their orientation and electronic properties to answer many difficult questions towards the performance of low-dimensional devices such as energy harvesting, advanced metal-oxide-semiconductor storage, nanoelectromechanical and nanophotonic devices.

Acknowledgements

The part of the work was carried out in the laboratories of Professor Jörg Enderlein. S.G. thanks the International Max Planck Research School for Physics of Biological and Complex Systems (IMPRS-PBCS) for awarding the MWR doctoral scholarship. The authors thank the Centre for Nano Science and Engineering, IISc, Bangalore and IVth Institute of Physics, University of Göttingen for the technical facilities. M.G. thanks ministry of human resource development (MHRD), the Government of India for her previous fellowship. The authors thank J.E. for supporting the work with the defocus imaging code, critical comments and plenty of scientific discussions.

References

1 S. R. Anton and H. A. Sodano, Smart Mater. Struct., 200[illegible] **16**, R1.
2 X. Chen, S. Xu, N. Yao and Y. Shi, Nano Lett., 2010, **10**, 21[illegible]
3 M. Ghosh and G. M. Rao, Mater. Express, 2013, **3**, 319.
4 Y. C. Yang, C. Song, X. H. Wang, F. Zeng, and F. Pan, A[illegible] Phys. Lett., 2008, **92**, 012907.
5 Y. H. Lin, M. Ying, M. Li, X. Wang and C. W. Nan, Appl. Phys. Lett., 2007, **90**, 222110.
6 T. M. Babinec, B. J. M. Hausmann, M. Khan, Y. Zhang, J. R. Maze, P. R. Hemmer and M. Lončar, Nat. Nanotechnol. 2010, **5**, 195.
7 X. J. Wang, I. A. Buyanova, F. Zhao, D. Lagarde, A. Balocchi, X. Marie, C. W. Tu, J. C. Harmand and W. M. Chen, Nature Mater., 2009, **8**, 198.
8 F. Fabbri, M. Villani, A. Catellani, A. Calzolari, G. Cicero, D. Calestani, G. Calestani, A. Zappettini, B. Dierre, T. Sekiguchi and G. Salviati, Sci. Rep., 2014, **4**, 5158.
9 F. D. Angelis and A. Armelao, Phys. Chem. Chem. Phys., 2011, **13**, 467.
10 A. Janotti and C. G. Van de Walle, Phys. Rev. B Condens. Matter., 2007, **76**, 165202.
11 H. J. Kimble, M. Dagenais and L. Mandel, Phys. Rev. Lett. 1977, **39**, 691.
12 B. Lounisa, H. A. Bechtel, D. Gerion, P. Alivisatos and W. E. Moerner, Chem. Phys. Lett., 2000, **329**, 399.
13 S. Choi, A. M. Berhane, A. Gentle, C. Ton-That, M. R. PhillipsIgor and I. Aharonovich, ACS Appl. Mater. Interfaces, 2015, **7**, 5619.
14 N. R. Jungwirth, Y. Y. Pai, H. S. Chang, E. R. MacQuarrie, K. X. Nguyen and G. D. Fuchs, J. Appl. Phys., 2014, **116**, 043509.
15 O. Neitzke, A. Morfa, J. Wolters, A. W. Schell, G. Kewes and O. Benson, Nano Lett., 2015, **15**, 3024.
16 D. Patra, I. Gregor and J. Enderlein, J. Phys. Chem. A, 2004, **108**, 6836.
17 M. A. Lieb, J. M. Zavislan and L. Novotny, J. Opt. Soc. Am. B., 2004, **21**, 1210.
18 D. Patra, I. Gregor, J. Enderlein and M. Sauer, Appl. Phys. Lett., 2005, **87**, 101103.
19 T. Li, Q. Li, Y. Xu, X. J. Chen, Q. F. Dai, H. Liu, S. Lan, S. Tie and L. J. Wu, ACS Nano, 2012, **6**, 1268.
20 J. A. Hutchison, H. Uji-i, A. Deres, T. Vosch, S. Rocha, J. Müller, A. A. Bastian, J. Enderlein, H. Nourouzi, C. Li, A. Herrmann, K. Müllen, F. D. Schryver and J. Hofkens, Nat. Nanotechnol., 2014, **9**, 131.
21 J. Enderlein, T. Ruckstuhl and S. Seeger, Appl. Opt., 1999, **38**, 724.

22 L. K. V. Vugt, S. Rühle, P. Ravindran, H. C. Gerritsen, L. Kuipers, and D. Vanmaekelbergh, Phys. Rev. Lett., 2006, **97**, 147401.
23 A. V. Dijken, E. A. Meulenkamp, D. Vanmaekelbergh, and A. Meijerink, J. Lumin., 2000, **87**, 454.
24 J. Lähnemann, U. Jahn, O. Brandt, T. Flissikowski, P. Dogan and H. T. Grahn, J. Phys. D: Appl. Phys., 2014, **47**, 423001.
25 V. A. Fonoberov and A. A. Balandin, Phys. Rev. B, 2004, **70**, 195410.
26 M. G. Bawendi, P. J. Carroll, W. L. Wilson and L. E. Brus, 1992, J. Chem. Phys., 1992, **96**, 946.
27 H. Jönen, U. Rossow, H. Bremers, L. Hoffmann, M. Brendel, A. D. Dräger, S. Schwaiger, F. Scholz, J. Thalmair, J. Zweck and A. Hangleiter, Appl. Phys. Lett., 2011, **99**, 011901.
28 S. Guha, J. M. DePuydt, J. Qiu, G. E. Hofler, M. A. Haase, B. J. Wu and H. Cheng, Appl. Phys. Lett., 1993, **63**, 3023.
29 R. Liu, A. Bell, F. A. Ponce, C. Q. Chen, J. W. Yang and M. A. Khan, Appl. Phys. Lett., 2005, **86**, 021908.
30 J. Hu, L. Li, W. Yang, L. Manna, L. Wang and A. P. Alivisatos. Science, 2001, **292**, 2060.
31 D. C. Look, R. C. Scott, K. D. Leedy and B. Bayraktaroglu. SPIE OPTO, pp. 794003-794003. International Society for Optics and Photonics, 2011.
32 H. P. Sun, X. Q. Pan, X. L. Du, Z. X. Mei, Z. Q. Zeng and Q. K. Xue, Appl. Phys. Lett., 2004, **85**, 4385.

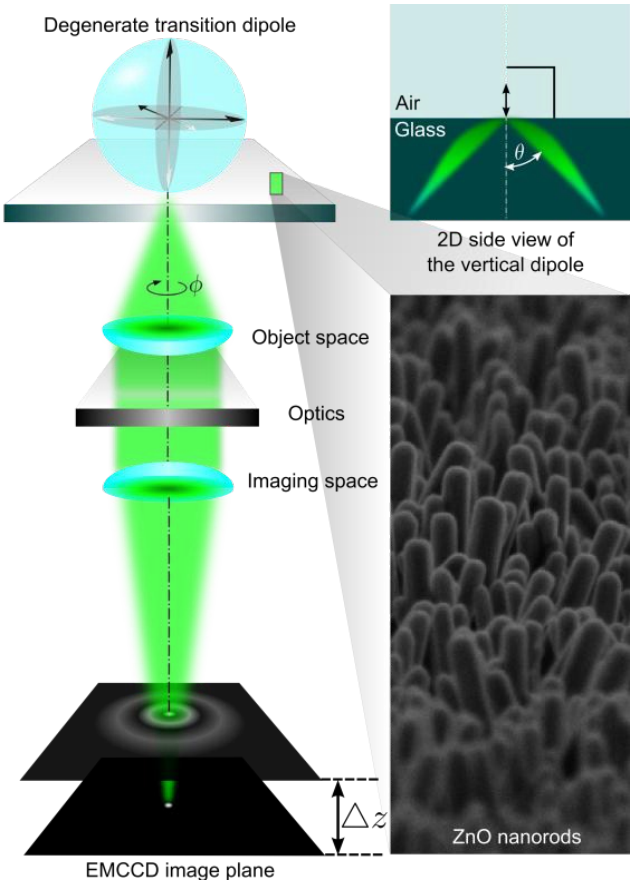

TOC entry